Scanning-probe-microscopy studies of superlattice structures and density-wave structures in 2H-$NbSe_2$, 2H-$TaSe_2$, and 2H-TaS_2 induced by Fe doping

Z. Dai, Q. Xue, Y. Gong, C. G. Slough, and R. V. Coleman
Physics Department, University of Virginia, Charlottesville, Virginia 22901
(Received 5 April 1993)

The intercalation of Fe into the van der Waals gap in the 2H phase transition-metal dichalcogenides $NbSe_2$, $TaSe_2$, and TaS_2 produces many interesting electronic, magnetic, and structural effects. The scanning tunneling microscope (STM) and atomic force microscope (AFM) prove to be very sensitive to these changes and we report a wide range of results as a function of Fe concentration. All three materials support similar $3\mathbf{a}_0\times3\mathbf{a}_0$ charge-density-wave (CDW) structures in the pure state at low temperatures. At low concentrations of Fe the CDW superlattice is still strong at 4.2 K and persists to high concentrations of Fe. At high concentrations, the Fe becomes ordered in the octahedral holes in the van der Waals gaps, and superlattices of the form $2\mathbf{a}_0\times2\mathbf{a}_0$ and $\sqrt{3}\mathbf{a}_0\times\sqrt{3}\mathbf{a}_0$ are observed. These can be detected at both 300 and 4.2 K. STM spectroscopy at 4.2 K shows that in 2H-$Fe_x NbSe_2$ and 2H-$Fe_x TaSe_2$ the energy gap in the electronic spectrum is initially reduced, but stabilizes at higher Fe concentrations and remains well defined for the ordered $2\mathbf{a}_0\times2\mathbf{a}_0$ phase. A transition from a CDW to a mixed CDW and spin-density-wave state is indicated, since these high Fe concentration phases are antiferromagnetic. In 2H-$Fe_x TaS_2$ both $2\mathbf{a}_0\times2\mathbf{a}_0$ and $\sqrt{3}\mathbf{a}_0\times\sqrt{3}\mathbf{a}_0$ superlattices are observed. The $2\mathbf{a}_0\times2\mathbf{a}_0$ regions show a large energy gap, while the $\sqrt{3}\mathbf{a}_0\times\sqrt{3}\mathbf{a}_0$ do not. The latter phase is ferromagnetic and would not be expected to exhibit a gap. The development of the electronic structures over the entire range of Fe concentrations has been followed by STM and AFM and can be tracked in detail.

I. INTRODUCTION

We have used scanning tunneling microscopes (STM's) operating at 4.2 and 300 K and atomic force microscopes (AFM's) operating at 300 K to study the intercalation of Fe into the van der Waals gap of the 2H phase of the transition-metal dichalcogenides[1] $NbSe_2$, $TaSe_2$, and TaS_2. At low temperatures the pure materials support charge-density waves[2] (CDW's) which partially gap the Fermi surfaces, but the CDW phases remain metallic at the lowest temperatures. The intercalation of Fe into the van der Waals gap gradually modifies the CDW structure in all three materials, but the CDW structure persists on a microscopic scale up to high Fe concentrations of 20% or more. The Fe atoms occupy the octahedral holes between the chalcogen atoms and at higher concentrations form ordered superlattices. The ordered superlattices produce either antiferromagnetic or ferromagnetic transitions with onset temperatures below room temperature.

The Fe atoms create charge transfer to the sandwich layers and this allows both the STM and AFM to detect the formation of the superlattice. The form of the superlattice can be a function of Fe concentration and in some intercalated crystals two types of superlattice can be observed due to microscopic variation in the Fe occupation of the octahedral holes.

Using a low-temperature STM we have also measured the effect of Fe concentration on the CDW energy gaps. These can change rapidly in certain ranges of Fe concentration, but remain relatively large up to high Fe concentrations. In addition, the crystals that exhibit antiferromagnetic phases continue to exhibit a gap in the energy spectrum, so that the CDW energy gap merges continuously into a gap characterizing the antiferromagnetic phase which indicates the existence of a mixed density-wave state throughout the range of Fe concentration.

At higher concentrations of Fe ordered superlattices and magnetic phases can be observed. In 2H-$Fe_x NbSe_2$ the magnetic phase is antiferromagnetic and the superlattice is $2\mathbf{a}_0\times2\mathbf{a}_0$. A $2\mathbf{a}_0\times2\mathbf{a}_0$ superlattice is also observed in 2H-$Fe_x TaSe_2$ while in 2H-$Fe_x TaS_2$ superlattices of $\sqrt{3}\mathbf{a}_0\times\sqrt{3}\mathbf{a}_0$ and $2\mathbf{a}_0\times2\mathbf{a}_0$ can be observed in different crystals or in different areas of the same crystal. The 2H-$Fe_{0.33}TaS_2$ crystals with a $\sqrt{3}\mathbf{a}_0\times\sqrt{3}\mathbf{a}_0$ superlattice are ferromagnetic below ~80 K and exhibit no gap in the energy spectrum while 2H-$Fe_x TaS_2$ crystals with a $2\mathbf{a}_0\times2\mathbf{a}_0$ superlattice exhibit a well-defined energy gap at 4.2 K.

We have carried out STM and AFM scans on crystals with Fe concentrations in the range $x=0$–0.33. STM spectroscopy has been performed at 4.2 K and, in addition to energy gaps, a number of features indicating coupling to the Fe or to excitations of the magnetic phase have been observed. In some spectra from 2H-$Fe_{0.33}NbSe_2$ crystals, zero bias peaks in conductance indicate an interaction of the tunneling electrons with Fe atoms at or close to the surface. In some cases isolated Fe or FeO_x particles can produce Coulomb barrier effects. At higher energies strong peaks in conductance indicate a resonance coupling to the magnetic phase. STM and AFM scans showing superlattice formation in all three 2H phase materials will be shown along with spectroscopy curves that track the energy gap associated with the density waves.

0163-1829/93/48(19)/14543(13)/$06.00 ©1993 The American Physical Society

Results of STM and AFM studies on the pure transition-metal dichalcogenides have been reviewed by Coleman and co-workers.[3,4]

II. EXPERIMENTAL TECHNIQUES

The STM's used in these experiments include both custom built and commercial models. The custom built STM's are designed to operate in a cryogenic environment and are all based on a similar design briefly described below and in greater detail in Refs. 3 and 4. Operating with the microscope submersed in a cryogenic liquid has produced a high degree of thermal stability and has greatly aided in the detection of the many subtle electronic effects observed. Room-temperature STM and AFM images were obtained with Nanoscope II and III scanning probe miroscopes built by Digital Instruments.[5]

The custom built STM's used in these experiments follow a simple basic design using an x-y translator cut from a single block of Channel 5400 piezoelectric material (Channel Industries, Santa Barbara, CA) and a semicircular disk bimorph made of Channel 5800 material. The tunneling tip is mounted in the x-y translator and the crystal is mounted on the bimorph which provides the z deflection.

All images produced by the cryogenic STM were taken in the constant current mode. The tunneling currents were typically 1–10 nA and the tunneling bias voltages were in the range 10–100 mV. Spectroscopic curves were obtained by momentarily interrupting the feedback loop to the microscope and sweeping the bias voltage through the designated range. The current was recorded directly to give an I versus V plot. The dI/dV versus V curves were recorded by applying an additional ac signal of 3 mV and 1 kHz during the dc sweep. The magnitude of the conductance was detected with a lock-in amplifier.

The transition-metal dichalcogenides studied in this paper were grown by the method of iodine vapor transport. For the pure crystals, stoichiometric quantities of powder were sealed in quartz tubes and prereacted by sintering at 900 °C. The sintered powders were then sealed in another quartz tube with iodine gas and placed in an oven. The exact temperature and temperature gradients differ for each compound. The crystals are slowly cooled from temperatures around 750 °C. High-quality crystals resulted from these growth procedures, as confirmed by residual resistance ratios **R** of 60 to 300, and the observation of large magnetoquantum oscillations in the pure 2H compounds. The Fe enters the van der Waals gaps in the single crystals grown from the sin-

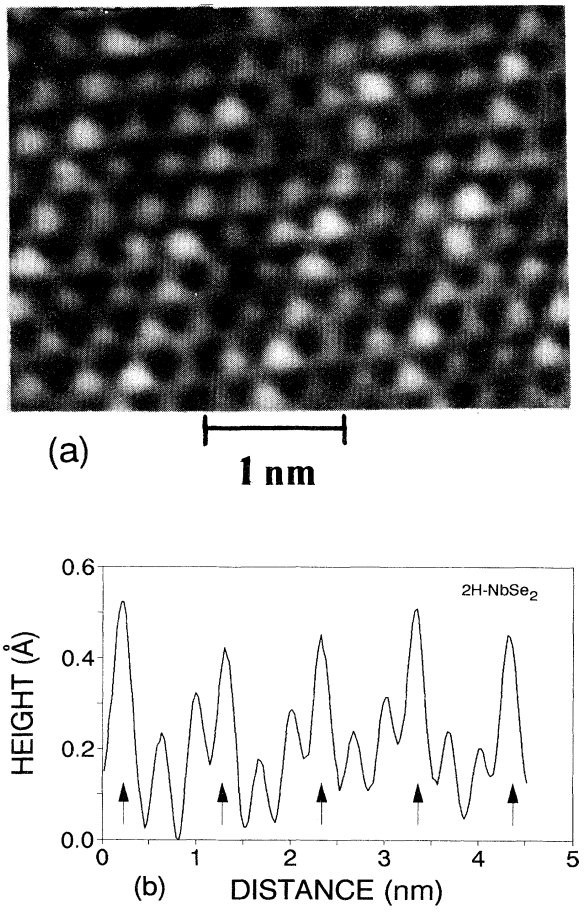

FIG. 1. (a) STM gray scale image of 2H-$NbSe_2$ recorded at 4.2 K (2 nA, 50 mV). This shows a $\sim 3\mathbf{a}_0 \times 3\mathbf{a}_0$ CDW superlattice. (b) Profile of z deflection along a line of atoms in (a). The total z deflection is ~ 0.5 Å with the CDW and atomic modulations showing approximately equal magnitudes (from Ref. 4).

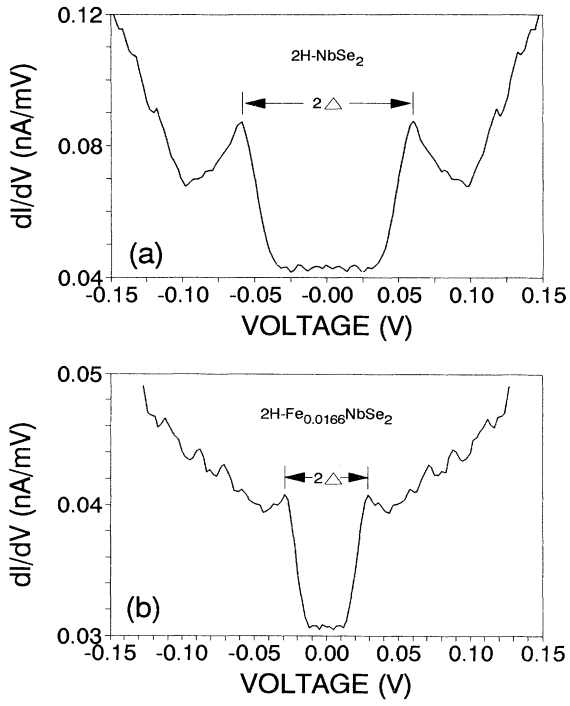

FIG. 2. Conductance vs bias-voltage curves measured at 4.2 K. The arrows indicate the conductance peaks above the CDW gap edges. (a) Pure 2H-$NbSe_2$ with peaks at $\sim \pm 59.0$ mV. (b) 2H-$Fe_{0.0166}NbSe_2$ shows peaks at $\sim \pm 31.0$ mV. The magnitude is reduced by $\sim 50\%$ compared to the pure phase in (a).

tered powders and little if any incorporates in the close-packed layers of the crystals. At the higher Fe concentrations the Fe begins to order on the octahedral hole sites within the van der Waals gap.

For the Fe-doped crystals, the appropriate amount of Fe powder was added and sintered along with the pure quantities. Ordered regions of a $2\mathbf{a}_0 \times 2\mathbf{a}_0$ superlattice correspond to a local Fe concentration of $x = 0.25$ while ordered regions of a $\sqrt{3}\mathbf{a}_0 \times \sqrt{3}\mathbf{a}_0$ superlattice correspond to a local Fe concentration of $x = 0.33$.

III. EXPERIMENTAL RESULTS K

A. STM of $Fe_x NbSe_2$ at 4.2 K

Pure 2H-$NbSe_2$ exhibits an incommensurate CDW below 35 K with a wavelength of $\sim 3a_0$. The $\mathbf{q}$ vector[6] is given by $\mathbf{q} = (1-\delta)a^*/3$ with $\delta = 0.025$ at the CDW onset and $\delta = 0.011$ at 5 K. Figure 1(a) shows a STM scan of pure 2H-$NbSe_2$ at 4.2 K showing the $3\mathbf{a}_0 \times 3\mathbf{a}_0$ CDW superlattice as well as the atomic lattice. The total z deflection is ~ 0.5 Å equally divided between the atom deflection and the CDW deflection as shown in the profile of Fig. 1(b).

The STM spectroscopy of pure 2H-$NbSe_2$ shows gap edges at ± 59.0 mV as shown in Fig. 2(a). The addition of Fe to 2H-$NbSe_2$ at a concentration on the order of 1% substantially reduces the measured CDW energy gap as shown in Fig. 2(b) for $x = 0.0166$. The gap edges are observed at ± 31.0 mV. In this low range of Fe concentrations the CDW amplitude shows only small changes and the STM scans continue to show a strong $3\mathbf{a}_0 \times 3\mathbf{a}_0$ superlattice. The resistance versus temperature develops a Kondolike resistance minimum[7] as shown in Fig. 3(a) and this continues to be observed for Fe concentrations in excess of 10% as shown in Fig. 3(b). As shown in the profiles of Figs. 4(a) and 4(b) the CDW modulation of wavelength $3\mathbf{a}_0$ continues to dominate in this range of Fe concentration. At Fe concentrations above $x = 0.10$ the $3\mathbf{a}_0$ modulation is still observed as shown in Fig. 4(c), but the total z deflection becomes considerably larger than observed in pure 2H-$NbSe_2$ or in 2H-$NbSe_2$ with dilute Fe doping.

As the Fe concentration increases the $3\mathbf{a}_0 \times 3\mathbf{a}_0$ super-

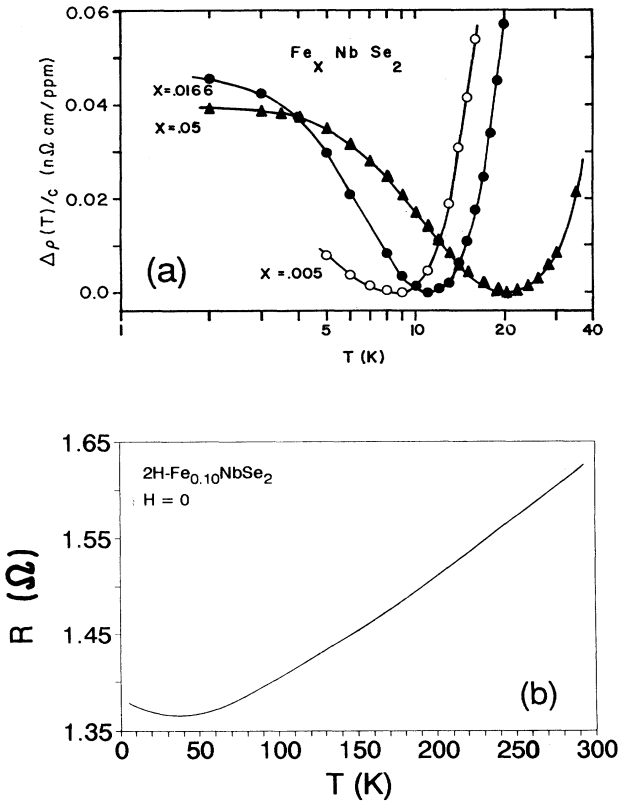

FIG. 3. (a) Temperature dependence of the resistivity change $\Delta\rho$ parallel to the layers divided by the Fe concentration c. The Kondolike minima are obtained for all three doped 2H-$NbSe_2$ compounds. The position of the minimum shifts to higher temperatures as the concentration increases (from Ref. 7). (b) The resistance vs temperature curve measured parallel to the layers of 2H-$Fe_{0.10}NbSe_2$ again shows a Kondolike minimum with the position of the minimum at ~ 35 K.

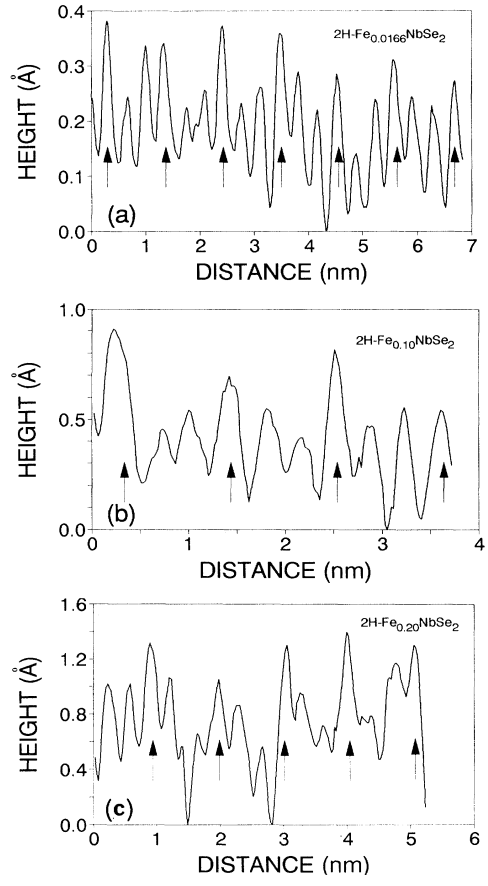

FIG. 4. Profiles of z deflection taken from STM images at 4.2 K for (a) 2H-$Fe_{0.0166}NbSe_2$, (b) 2H-$Fe_{0.10}NbSe_2$, and (c) 2H-$Fe_{0.20}NbSe_2$. All three profiles show the $\sim 3\mathbf{a}_0 \times 3\mathbf{a}_0$ CDW modulation, which is dominant in (a) and (b). The amplitude of the CDW modulation increases with increasing concentration of Fe.

lattice becomes more disordered in the STM scans, but the CDW gap decreases only very slowly with the gap edges observed at 28.0 ± 3.4 mV for $x=0.10$ and at 25.4 ± 1.0 mV for $x=0.20$ as shown in Figs. 5(a) and 5(b). In the Fe concentration range of $x=0.20-0.30$ the $3\mathbf{a}_0\times3\mathbf{a}_0$ superlattice disappears in the STM scans and is replaced by a $2\mathbf{a}_0\times2\mathbf{a}_0$ superlattice as shown in the scan and profile of Fig. 6. This coincides with the expected ordered occupancy of the octahedral hole sites in the van der Waals gap and the regions of perfect ordered $2\mathbf{a}_0\times2a_0$ superlattice occupancy would correspond to $x=0.25$. As shown in the profile of Fig. 6(b), the $2\mathbf{a}_0$ modulation is dominant and corresponds to an enhanced z deflection of ~2 Å. These observations suggest a substantial charge transfer from the Fe to the Nb atoms above the occupied octahedral sites as well as to the surface Se atoms.

Above $x=0.20$ the resistance versus temperature also makes a transition from the Kondolike behavior to curves showing a strong slope change in the neighborhood of 120 K and a monotonic decrease of resistance below this temperature. We associate this with the transition to an antiferromagnetic phase which is consistent with the susceptibility measurements reported by Hellenius and Coleman.[8] A resistance versus temperature plot for $x=0.33$ is shown in Fig. 7. At the same time STM spectroscopy measurements show that the energy gap persists and is essentially unchanged in magnitude as x increases from 0.20 to 0.33. As shown in Fig. 5(c) the gap edges are observed at $\pm25.3\pm1.5$ mV for $x=0.33$, the same magnitude as observed for $x=0.20$ in the spectrum of Fig. 5(b).

The STM spectroscopy also shows the existence of a strong resonance interaction with strong peaks in the conductance curves at ±150 mV as shown in Fig. 8(a) for $x=0.33$. This suggests possible interactions with the antiferromagnetic spin wave excitations. These strong resonance peaks can be observed at different positions on the crystal surface, but shift slightly in energy and at some locations can show a distinct splitting as shown in Fig. 8(b). Variations in the local occupancy of the octahedral holes by Fe may account for these spatial variations in resonance coupling in 2H-$Fe_{0.33}NbSe_2$.

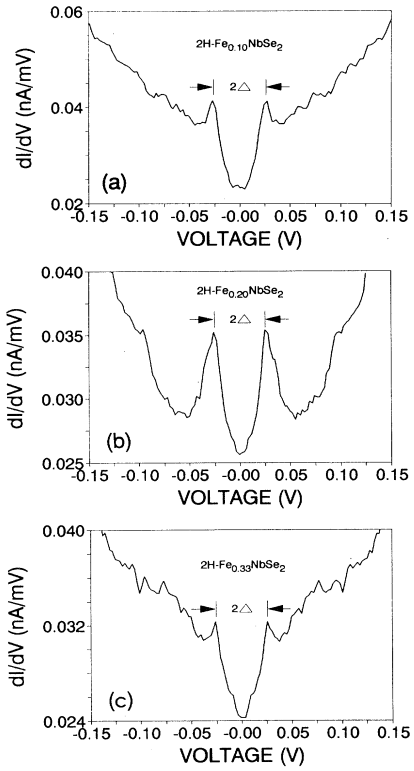

FIG. 5. Conductance vs bias-voltage curves measured at 4.2 K for 2H-Fe_xNbSe_2. They indicate that the CDW gap size remains relatively constant when the concentration of Fe is greater than $x=0.10$. (a) for $x=0.10$, $\Delta=28.0\pm3.4$ meV. (b) For $x=0.20$, $\Delta=25.4\pm1.0$ meV. (c) For $x=0.33$, $\Delta=25.3\pm01.5$ meV.

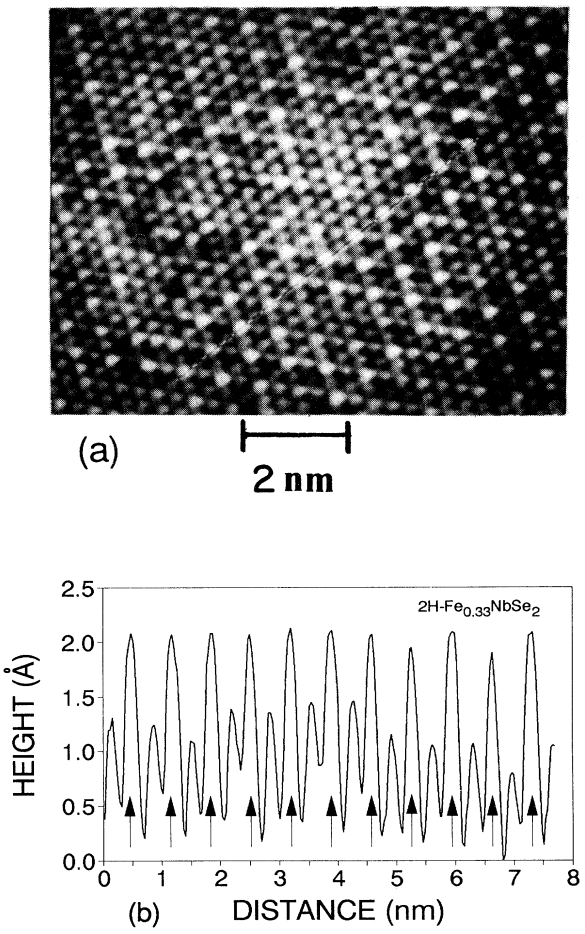

FIG. 6. (a) STM gray scale image of 2H-$Fe_{0.33}NbSe_2$ recorded at 4.2 K (2 nA, 50 mV). A $2\mathbf{a}_0\times2\mathbf{a}_0$ superlattice is clearly seen, which indicates that the $\sim3\mathbf{a}_0\times3\mathbf{a}_0$ CDW superlattice is reduced or converted to a mixed density wave. (b) Profile of z deflection along the line shown in (a). The total z deflection is ~2 Å with superlattice and atomic modulations of approximately equal amplitudes. However, these are much larger than those observed for pure 2H-$NbSe_2$.

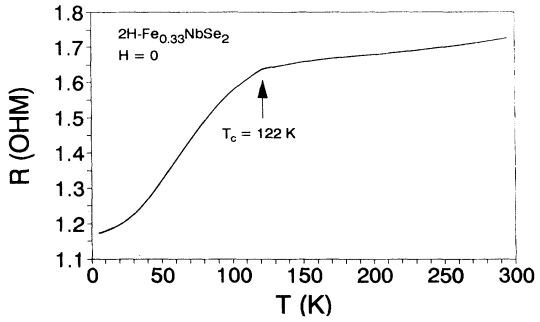

FIG. 7. Resistance vs temperature curve measured for 2H-$Fe_{0.33}NbSe_2$ which indicates an antiferromagnetic phase transition at ~122 K.

B. STM and AFM of $Fe_x NbSe_2$ at 300 K

Pure 2H-$NbSe_2$ exhibits a perfect atomic lattice at room temperature in both STM and AFM scans. The addition of intercalated Fe in the van der Waals gap is not detected at low concentrations on the order of $x=0.01$, but at much higher concentrations above $x=0.10$ local areas of $2\mathbf{a}_0 \times 2\mathbf{a}_0$ modulation gradually develop. At $x=0.33$ the crystals show a strong $2\mathbf{a}_0 \times 2\mathbf{a}_0$ superlattice as shown in the STM scan of Fig. 9(a). The scan shows an enhanced z deflection predominantly centered on every other Se atom with a slight asymmetry emphasizing two additional surface Se atoms in the seven-atom cluster to give a three-atom cluster. As shown in the profile of Fig. 9(b) the total z deflection is ~0.4 Å, with the additional $2\mathbf{a}_0$ modulation associated with the charge transfer from the Fe contributing more than half the total.

The AFM scan as shown in Fig. 10(a) exhibits the same basic response giving rise to a three-atom cluster with the center Se atom showing the greatest z deflection. As shown in the profile of Fig. 10(b) the total deflection is approximately 0.5 Å with about one half the deflection contribution by charge transfer to the center Se atom. Comparison of the STM and AFM scans suggests that the local density of states (LDOS) is more concentrated on the center Se atom while the combined effects on the total charge due to the charge transfer and Fermi surface

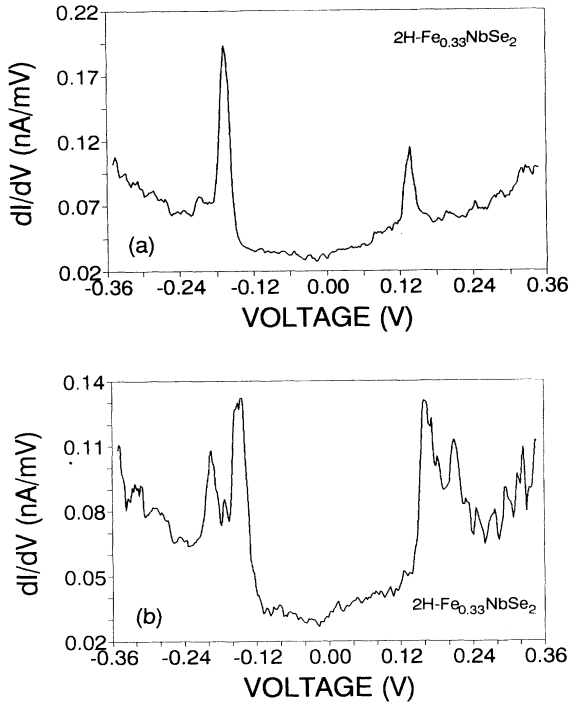

FIG. 8. Strong, sharp resonance peaks are observed in the conductance curves at ~±150 mV for 2H-$Fe_{0.33}NbSe_2$ at 4.2 K. (a) Peaks without splitting. (b) Peaks with splitting. The resonant peaks represent coupling to excitations of the Fe superlattice.

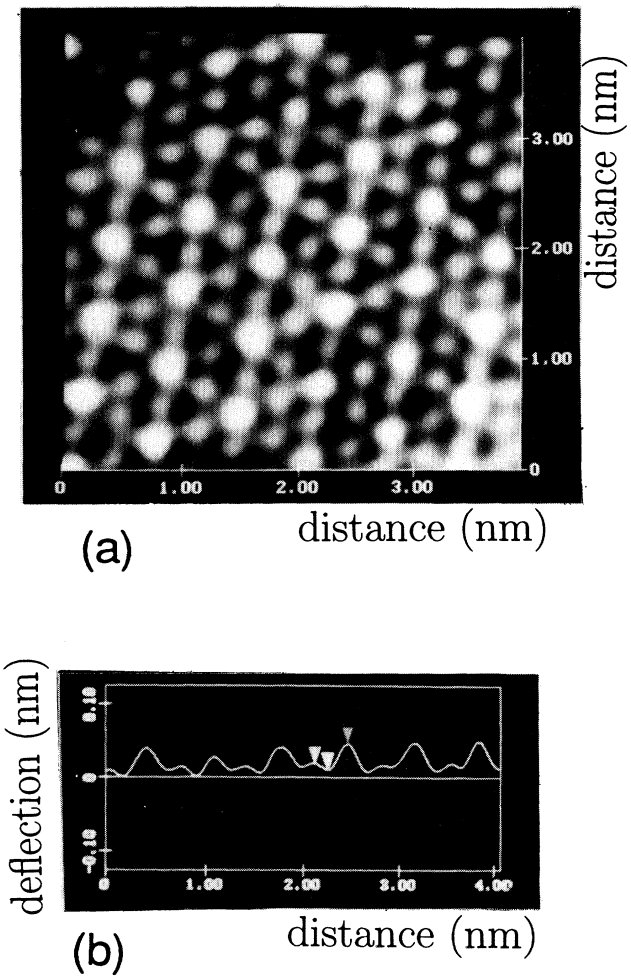

FIG. 9. (a) Gray scale image of STM scan at room temperature on 2H-$Fe_{0.33}NbSe_2$. The image was recorded using the constant current mode with $V=20$ mV and $I=6$ nA. The image indicates enhanced amplitude on every other Se atom with a slight asymmetry emphasizing two additional surface Se atoms in the seven atom cluster. (b) Profile of z deflection along a row of atoms in (a).

changes shift the response farther off the center Se atom as demonstrated in the three dimensional AFM scan presented in Fig. 10(c). However, both the AFM and STM scans show that the dominant charge transfer occurs to the center Se atom, even though the octahedral holes occupied by Fe are located symmetrically with respect to the three surface Se atoms. The nature of the charge transfer will be considered in Sec. IV.

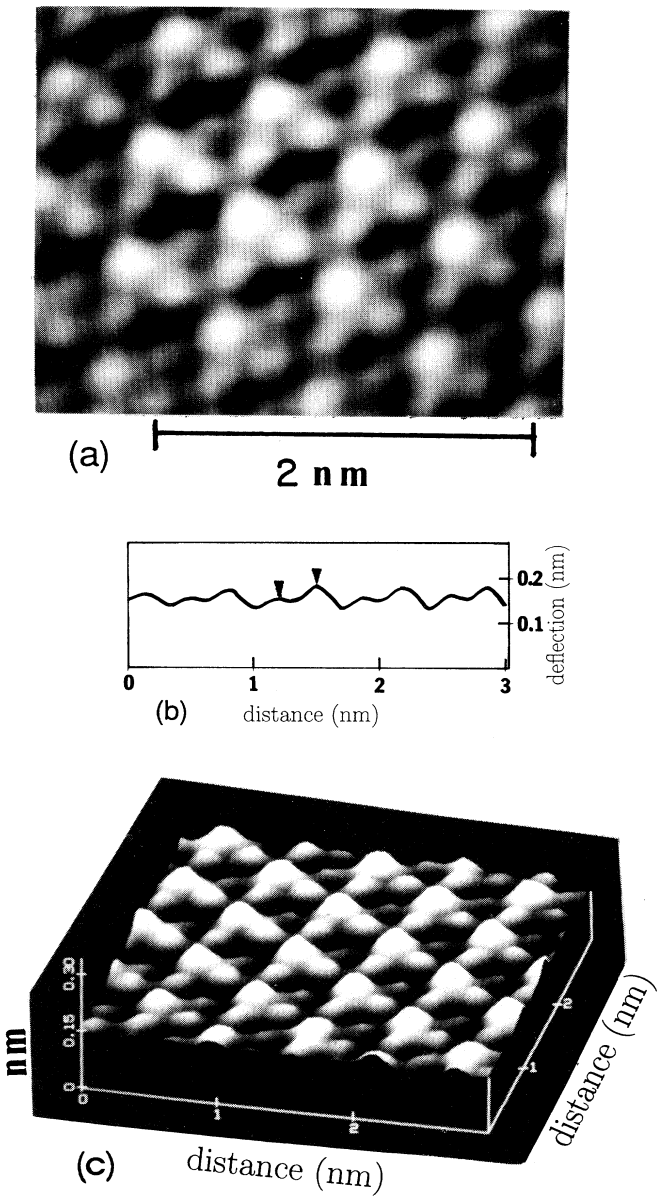

FIG. 10. (a) Gray scale image of AFM scan at room temperature on 2H-$Fe_{0.33}NbSe_2$. The image was recorded using the constant force mode. The image shows a basic $2\mathbf{a}_0 \times 2\mathbf{a}_0$ structure, but with a stronger three atom cluster than observed in the STM scan. (b) Profile of z deflection for the AFM scan of (a). The profile indicates that the atomic and superlattice deflections are comparable. (c) Three-dimensional projection of the AFM scan of (a). The strong three-atom cluster is clearly evident.

C. STM of $Fe_x TaSe_2$ at 4.2 K

The intercalation of Fe into the van der Waals gap of 2H-$TaSe_2$ produces a sequence of changes similar to those observed for 2H-$NbSe_2$. Pure 2H-$TaSe_2$ exhibits a CDW transition with an onset of 122.3 K. The CDW is initially incommensurate, but undergoes a first-order transition to a commensurate $3\mathbf{a}_0 \times 3\mathbf{a}_0$ superlattice at $\sim$90 K. At dilute Fe concentrations the $3\mathbf{a}_0 \times 3\mathbf{a}_0$ CDW superlattice modulation remains observable while the CDW energy gap undergoes an initial rapid reduction from $\sim$90 meV for pure 2H-$TaSe_2$ to $\sim$50 meV for $Fe_x TaSe_2$ with $x = 0.05$. Spectroscopy curves for $x = 0$ and 0.05 are shown in Fig. 11. In the lower ranges of Fe concentration a Kondolike minimum also develops in the resistance versus temperature curve followed by a resistance maximum as shown in Fig. 12(a).

At higher Fe concentrations the gap in the energy spectrum remains relatively unchanged in the range 50–60 meV and for $x = 0.33$ gives a value of 58.8 ± 4.6 mV for the location of the gap edge in the energy spectrum as shown in Fig. 13. Above $x = 0.20$ the resistance versus temperature curve also makes a transition to one exhibiting a sharp increase in slope below $\sim$58 K with a monotonic decrease to the lowest temperatures as shown in Fig. 12(b).

For Fe concentrations between $x = 0.20$ and 0.33 a $2\mathbf{a}_0 \times 2\mathbf{a}_0$ superlattice develops and is completely dominant at $x = 0.33$ as shown in the STM scan and profile of Fig. 14. The z deflection from the $2\mathbf{a}_0 \times 2\mathbf{a}_0$ superlattice remains small at $\sim$0.5 Å indicating that the charge

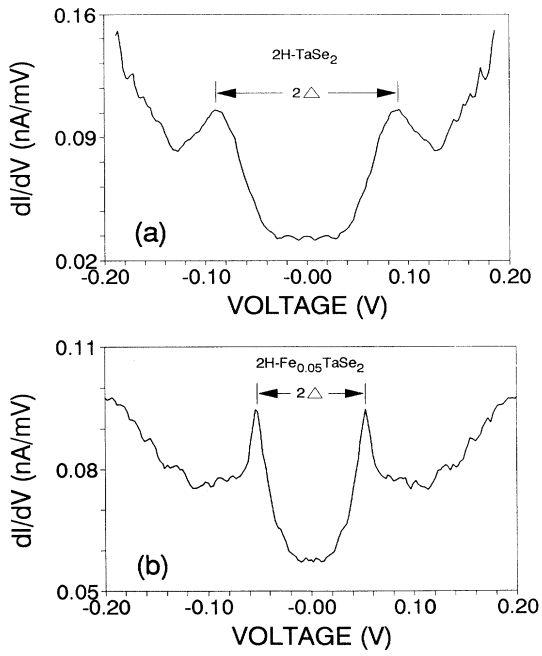

FIG. 11. Conductance vs bias-voltage curves measured at 4.2 K. (a) Pure 2H-$TaSe_2$ with peaks above CDW gap edges at $\sim \pm 89.9$ mV. (b) 2H-$Fe_{0.05}TaSe_2$ with peaks above CDW gap edges at $\sim \pm 54.6$ mV.

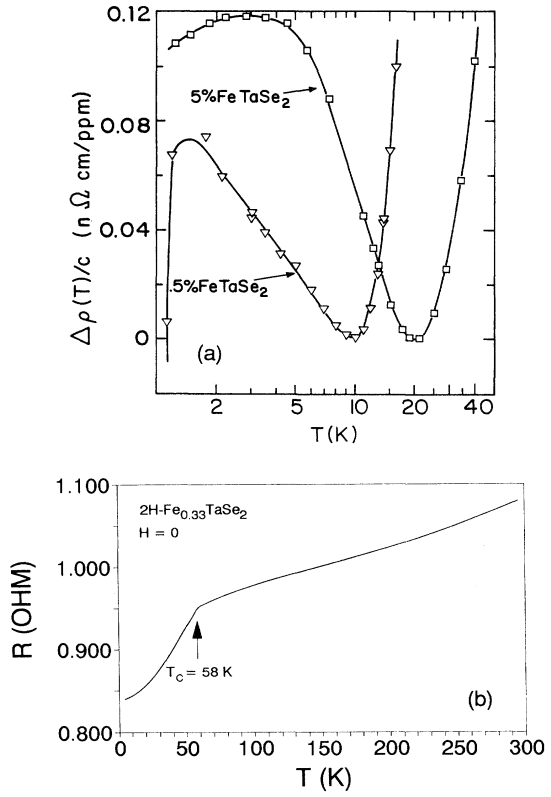

FIG. 12. (a) Temperature dependence of the resistivity change $\Delta\rho$ divided by the Fe concentration c, measured parallel to the layers for doped 2H-$TaSe_2$. A Kondolike minimum followed by a maximum is obtained for each of the two Fe-doped 2H-$TaSe_2$ crystals (from Ref. 7). (b) Resistance vs temperature curve measured for 2H-$Fe_{0.33}TaSe_2$. A magnetic phase transition is indicated at ~ 58 K.

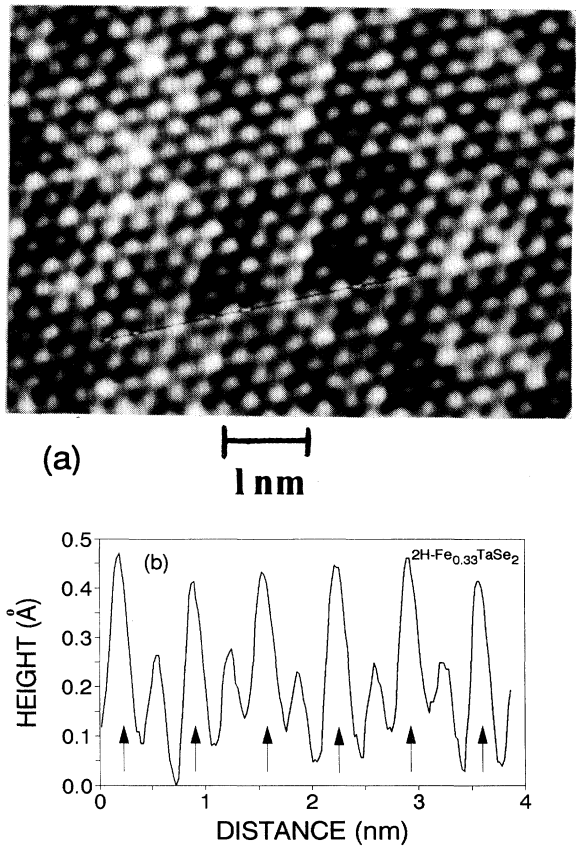

FIG. 14. (a) STM gray scale image of 2H-$Fe_{0.33}TaSe_2$ recorded at 4.2 K (2 nA, 50 mV). A $2\mathbf{a}_0 \times 2\mathbf{a}_0$ superlattice is clearly seen. (b) Profile of z deflection along the line shown in (a). The total z deflection is ~ 0.5 Å with superlattice and atomic modulations of approximately equal amplitudes.

transfer and change in LDOS due to Fe may be substantially less in 2H-$Fe_{0.25}TaSe_2$ than in 2H-$Fe_{0.25}NbSe_2$. The onset of the magnetic phase transition at ~ 58 K is also lower compared to the 122-K onset observed for 2H-$Fe_{0.25}NbSe_2$. Otherwise, the development of the $2\mathbf{a}_0 \times 2\mathbf{a}_0$ superlattice and magnetic phase follows the same pattern

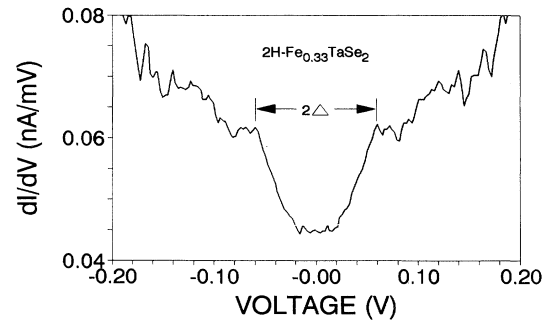

FIG. 13. Conductance vs bias-voltage curve measured at 4.2 K for 2H-$Fe_{0.33}TaSe_2$. The peaks above the gap edges occur at $\sim \pm 58.8$ mV.

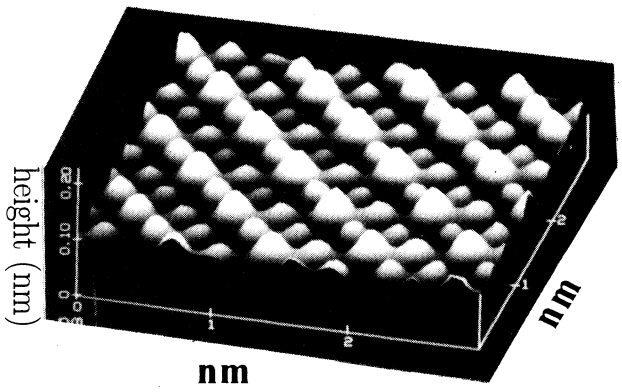

FIG. 15. Three-dimensional projection of an AFM scan at room temperature on 2H-$Fe_{0.33}TaSe_2$. The picture was recorded using the constant force mode. The picture indicates a clear $2\mathbf{a}_0 \times 2\mathbf{a}_0$ superlattice due to the Fe intercalation.

as a function of Fe concentration in both 2H-$Fe_x NbSe_2$ and 2H-$Fe_x TaSe_2$.

Measurements of the resistance versus temperature as analyzed in Ref. 7 show negative values of the exchange constant for both 2H-$Fe_x NbSe_2$ and 2H-$Fe_x TaSe_2$. We conclude that 2H-$Fe_x TaSe_2$ also develops an antiferromagnetic phase although susceptibility measurements at high Fe concentrations have not been made. The persistence of the energy gaps in the high Fe concentration phases of both 2H-$NbSe_2$ and 2H-$TaSe_2$ also appears to be characteristic of crystals that develop a $2\mathbf{a}_0 \times 2\mathbf{a}_0$ superlattice and exhibit antiferromagnetic phases. Further discussion will be given in Sec. IV.

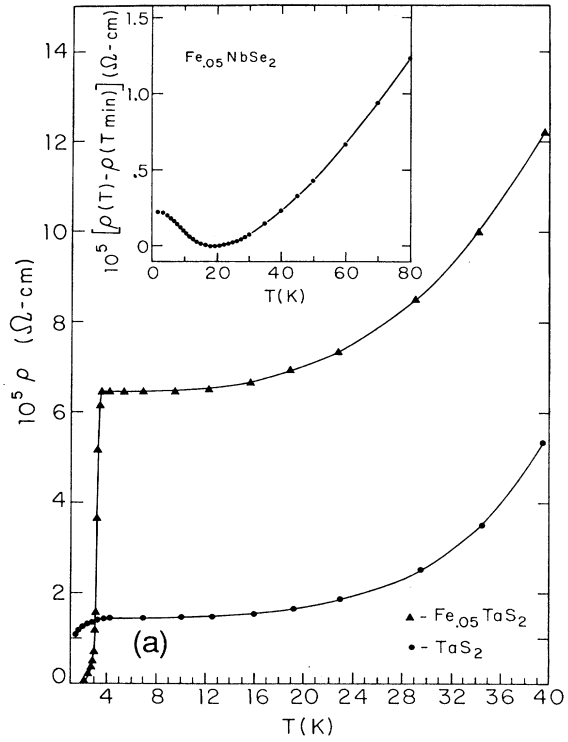

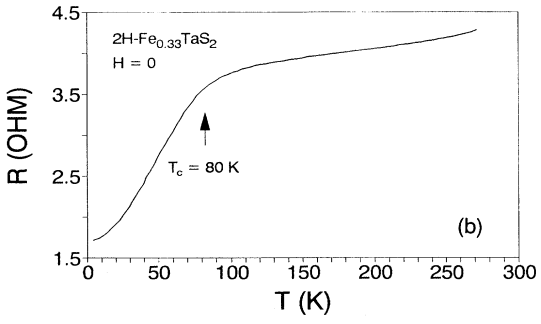

FIG. 16. (a) Resistivity vs temperature curves measured in the temperature range 1–40 K for 2H-TaS_2 and 2H-$Fe_{0.05}TaS_2$. The curve of 2H-$Fe_{0.05}TaS_2$ exhibits a superconducting transition at ~3 K and shows no Kondolike minimum. The pure material is superconducting only below 0.8 K. Insert shows $Fe_{0.05}NbSe_2$ for comparison. (b) Resistance vs temperature measured for 2H-$Fe_{0.33}TaS_2$. A magnetic transition is indicated at 80 K.

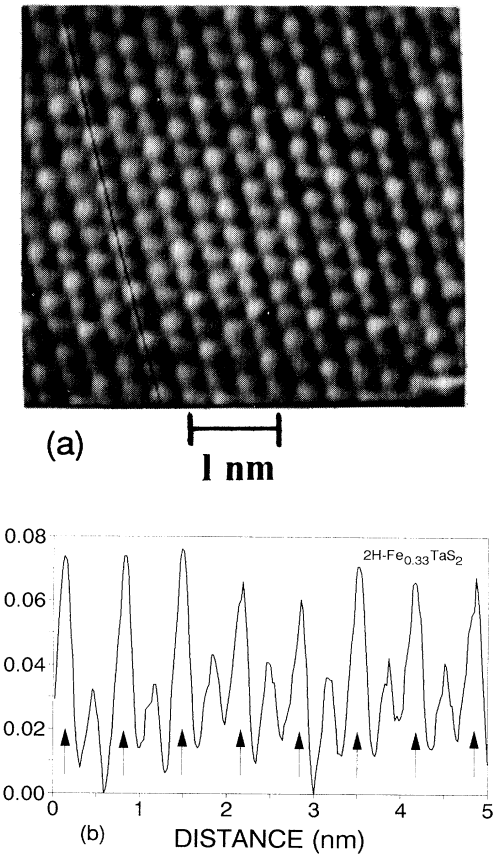

FIG. 17. (a) STM gray scale image of 2H-$Fe_{0.33}TaS_2$ recorded at 4.2 K (2 nA, 50 mV). A complete $2\mathbf{a}_0 \times 2\mathbf{a}_0$ superlattice is clearly seen. (b) Profile of z deflection along the line shown in (a). The total z deflection is ~0.07 Å with the superlattice and atomic modulations of approximately equal amplitudes. These are much weaker than observed for pure 2H-TaS_2.

D. STM and AFM of $Fe_x TaSe_x$ at 300 K

At 300 K the STM scans of 2H-$Fe_{0.33}TaSe_2$ show an extremely weak $2\mathbf{a}_0 \times 2\mathbf{a}_0$ modulation which is barely

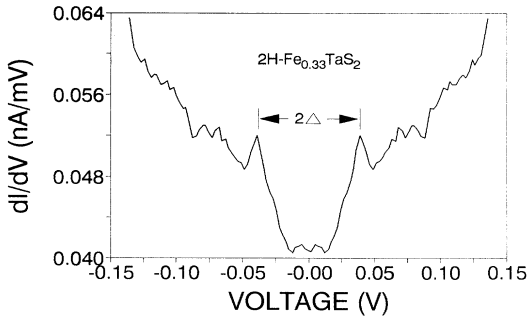

FIG. 18. Conductance vs bias-voltage curve measured at 4.2 K for 2H-$Fe_{0.33}TaS_2$. (a) The curve was measured on a crystal with a $2\mathbf{a}_0 \times 2\mathbf{a}_0$ superlattice and a clear energy gap structure with peaks in conductance at ~±38.3 meV is observed.

detectable relative to the atomic modulation by the surface Se atoms. This indicates that the LDOS at the Fermi level at the position of the STM tip has not been appreciably modified at room temperature while it is substantially modified below the magnetic transition at 58 K as was indicated in the STM scale at 4.2 K (see Fig. 14).

In contrast to the STM scans the AFM scans at room temperature show a much larger relative amplitude modulation at the $2\mathbf{a}_0$ wavelength. As shown in the three-dimensional AFM scan of Fig. 15, the added intensity is fairly well concentrated on the center Se atom of the seven atom cluster.

These results at room temperature on 2H-$Fe_{0.33}TaSe_2$ indicate that the static charge transfer to the surface Se atoms by the Fe superlattice and detected by the AFM is relatively large compared to the modification of the LDOS at the Fermi level induced by the Fe superlattice and detected by the STM at room temperature.

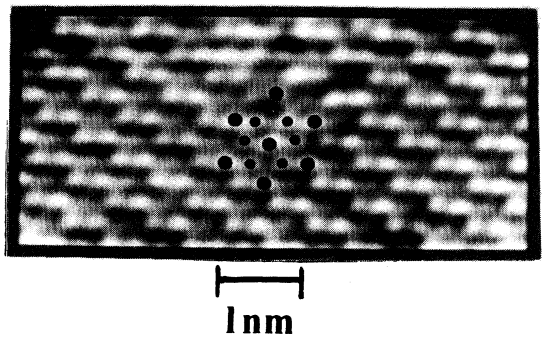

FIG. 19. STM gray scale image of 2H-$Fe_{0.33}TaS_2$ recorded at 4.2 K. A $\sqrt{3}\mathbf{a}_0\times\sqrt{3}\mathbf{a}_0$ superlattice is observed. The superlattice, marked by larger solid circles, appears as the larger hexagon rotated 30° from the inner atom hexagon (small solid circles).

E. STM of Fe_xTaS_2 at 4.2 K

The same series of Fe intercalated alloys of 2H-TaS_2 as were measured for Fe intercalated 2H-$NbSe_2$ and 2H-$TaSe_2$ have also been studied by both STM and AFM. In this case the electronic behavior is quite different and the STM and AFM techniques easily detect these differences. The 2H phase of TaS_2 exhibits a CDW onset at ~ 75 K and forms a $\sim 3\mathbf{a}_0\times 3\mathbf{a}_0$ superlattice that remains incommensurate down to at least 14 K. The measured wave vector at 70 K is given by $\mathbf{q}=(1+\delta)\mathbf{a}_0^*/3$ where $\delta=0.017\pm0.009$. At low concentrations of Fe with $x\leq 0.05$ the crystals become superconducting at ~ 3 K and no Kondolike minima are observed as shown in Fig. 16(a) for $x=0.05$. The STM scans also show the development of a $2a_0$ modulation in many regions of the crystal, although there is a mixture of $2\mathbf{a}_0$ and $3\mathbf{a}_0$ modulations in the STM scans. The CDW energy gap shows only a slow reduction as the Fe concentration is increased. The measured values for $x=0$, 0.05, and 0.08 are 55.5 ± 3.7, 52.6 ± 2.2, and 46.2 ± 2.7 meV indicating that the CDW phase remains relatively strong even though regions of ordered Fe occupation are forming.

At higher Fe concentrations regions of ordered superlattices of both $2\mathbf{a}_0\times2\mathbf{a}_0$ and $\sqrt{3}\mathbf{a}_0\times\sqrt{3}\mathbf{a}_0$ Fe occupancy of the octahedral holes are observed, and at $x=0.33$ the resistance versus temperature shows a transition at 80 K as shown in Fig. 16(b). A STM scan at 4.2 K showing a $2\mathbf{a}_0\times2\mathbf{a}_0$ superlattice is shown in Fig. 17(a) and a profile is shown in Fig. 17(b) for a crystal of $Fe_{0.33}TaS_2$. The local occupancy in this region is therefore $x=0.25$. The energy spectrum measured for a crystal with a $2\mathbf{a}_0\times2\mathbf{a}_0$ superlattice shows an energy gap of 38.3 ± 2.0 meV as calculated from the conductance curve shown in Fig. 18. In other regions of the same crystal or in different crystals a $\sqrt{3}\mathbf{a}_0\times\sqrt{3}\mathbf{a}_0$ superlattice can be observed in the STM scans at nominal Fe concentrations of $x=0.33$ as shown in Fig. 19. This indicates a local Fe concentration of $x\approx0.33$. The $\sqrt{3}\mathbf{a}_0\times\sqrt{3}\mathbf{a}_0$ superlattice appears as a larger hexagon rotated 30° from the inner hexagon of atoms in Fig. 19.

In the regions of the crystal with $\sqrt{3}\mathbf{a}_0\times\sqrt{3}\mathbf{a}_0$ superlattice the conductance curves show little or no evidence of any energy gap in the spectrum. Figure 20 shows a comparison of conductance curves measured from $\sqrt{3}\mathbf{a}_0\times\sqrt{3}\mathbf{a}_0$ versus $2\mathbf{a}_0\times2\mathbf{a}_0$ regions of the same crystal doped with an initial Fe concentration of $x=0.33$. The $\sqrt{3}\mathbf{a}_0\times\sqrt{3}\mathbf{a}_0$ superlattice in Fe_xTaS_2 with $x=0.28$ has previously been shown by Eibschütz *et al.*[9] to be ferromagnetic through the use of Mössbauer measurements. We conclude that this ferromagnetic phase does not exhibit an energy gap. The crystal regions with a $2\mathbf{a}_0\times2\mathbf{a}_0$ superlattice or crystals with a dominant $2\mathbf{a}_0\times2\mathbf{a}_0$ superlattice all show a substantial energy gap comparable to the energy gaps observed in the antiferromagnetic phases of 2H-Fe_xNbSe_2 and 2H-Fe_xTaSe_2.

The profiles of Fe_xTaS_2 in either phase show a weaker z deflection generated by the superlattice than is observed in Fe_xNbSe_2, 0.7 Å versus 2.0 Å. This indicates a weaker charge transfer from Fe, but otherwise the $2\mathbf{a}_0\times2\mathbf{a}_0$ su-

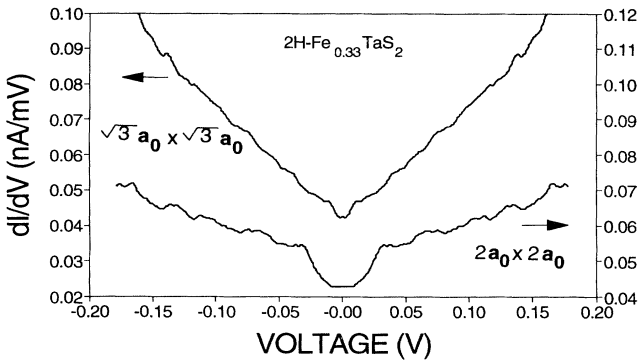

FIG. 20. Conductance vs voltage curves for 2H-$Fe_{0.33}TaS_2$ recorded at 4.2 K. Upper curve is an average of several curves taken with the STM tip over a $\sqrt{3}\mathbf{a}_0\times\sqrt{3}\mathbf{a}_0$ region of the crystal. Little or no gap structure is apparent. Lower curve is an average of several curves taken with the STM tip over a $2\mathbf{a}_0\times2\mathbf{a}_0$ region of the same crystal. An energy gap with a measured value of ~ 30 meV is present.

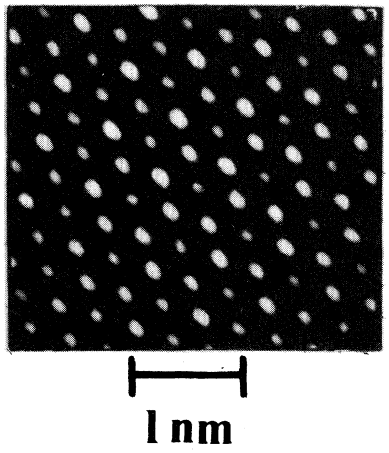

FIG. 21. Gray scale image of AFM scan at room temperature on 2H-$Fe_{0.33}TaS_2$. The image was recorded using the constant force mode. The upper region shows a large bright hexagon with an inner weaker hexagon rotated by 30°, while the lower region shows a large weak hexagon with an inner brighter hexagon rotated by 30°. This indicates a phase slip of the $\sqrt{3}\mathbf{a}_0\times\sqrt{3}\mathbf{a}_0$ superlattice, created by an increase in the local concentration of Fe in the octahedral holes.

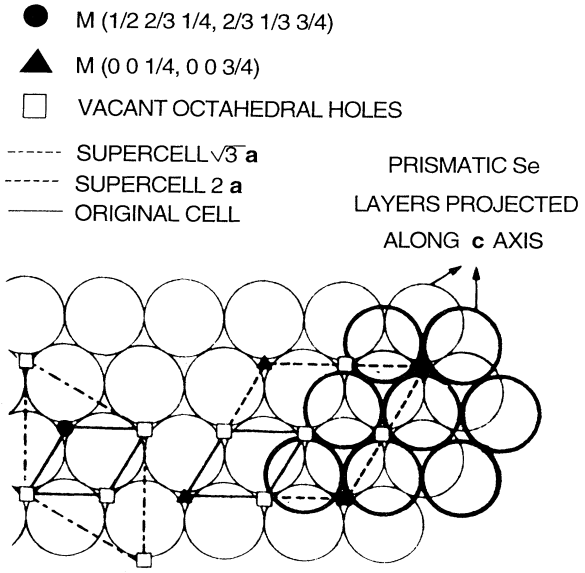

FIG. 22. Diagram of octahedral hole locations in 2H crystal structure. The two types of supercells are indicated by dashed lines.

perlattice is very similar to that observed in Fe_xNbSe_2 and Fe_xTaSe_2. Various aspects of the charge transfer and magnetic phase formation will be discussed in Sec. IV.

F. STM and AFM of Fe_xTaS_2 at 300 K

The $2\mathbf{a}_0\times2\mathbf{a}_0$ and $\sqrt{3}\mathbf{a}_0\times\sqrt{3}\mathbf{a}_0$ superlattices can be observed at room temperature in $Fe_{0.33}TaS_2$ using both STM and AFM. The charge transfer from Fe is relatively weak and the AFM gives the best resolution. The occupancy of the octahedral holes shows substantial variation such that regions of $2\mathbf{a}_0\times2\mathbf{a}_0$ and $\sqrt{3}\mathbf{a}_0\times\sqrt{3}\mathbf{a}_0$ can be observed in the same crystal for $x=0.33$. In addition, large regions of a single type of superlattice can also show variations in the configuration of the charge transfer to the surface S atoms. The entire region, however, remains in the $2\mathbf{a}_0\times2\mathbf{a}_0$ ordered superlattice state with a $2\mathbf{a}_0$ wavelength.

For crystals showing the $\sqrt{3}\mathbf{a}_0\times\sqrt{3}\mathbf{a}_0$ ordered superlattice in large regions, the Fe occupancy of the octahedral holes can show variations corresponding to a phase slip of the $\sqrt{3}\mathbf{a}_0\times\sqrt{3}\mathbf{a}_0$ superlattice. The relative height of the inner and outer hexagons similar to those in Fig. 19 are reversed. This reversal is equivalent to extra occupancy by Fe such that the $\sqrt{3}\mathbf{a}_0\times\sqrt{3}\mathbf{a}_0$ superlattice undergoes a phase slip of one octahedral hole spacing as shown from top to bottom in Fig. 21. The large and small hexagons in either case are rotated by 30°, which is a signature of the $\sqrt{3}\mathbf{a}_0\times\sqrt{3}\mathbf{a}_0$ superlattice.

IV. DISCUSSION

Previous x-ray-diffraction experiments[10,11] on 2H-Fe_xNbSe_2 and 2H-Fe_xTaS_2 have established the existence of ordered superlattices of Fe with the Fe atoms occupying the octahedral holes located below the Nb or Ta atoms as shown in Fig. 22. Occupancy of all of the available octahedral holes would correspond to $x=1.0$. In Fe_xNbSe_2 with $x=0.33$ the superlattice was observed to be $2\mathbf{a}_0\times2\mathbf{a}_0$ while with $x=0.50$ it was observed to be $\sqrt{3}\mathbf{a}_0\times\sqrt{3}\mathbf{a}_0$. The above values of x are those of the original growth compound used in the diffraction experiments. The regions of perfectly observed Fe superlattice correspond to $x=0.25$ and 0.33, respectively, while any additional Fe is either randomly distributed in octahedral holes or localized in clusters.

In the case of 2H-Fe_xTaS_2, the x-ray data for $x=0.33$ indicated the formation of a $\sqrt{3}\mathbf{a}_0\times\sqrt{3}\mathbf{a}_0$ superlattice. In both 2H-$NbSe_2$ and 2H-TaS_2 the addition of intercalated Fe was observed to expand the lattice along the c axis. In Fe_xNbSe_2 with $x=0.25$ and $x=0.33$ the lattice constants along the **c** axis were measured to be 12.62 and 12.67 Å, respectively, versus 12.54 Å in pure 2H-$NbSe_2$. The lattice constants in the plane of the layers showed only very small changes. In 2H-$Fe_{0.33}TaS_2$ the lattice constant in the **c** direction was measured to be 12.29 versus 12.10 Å in pure 2H-TaS_2. Lattice constants in the plane of the layers again showed very little change.

A. Superlattice formation and STM spectroscopy of 2H-Fe_xNbSe_2

The STM and AFM results reported in this paper for 2H-Fe_xNbSe_2 confirm the Fe superlattice structure as reported in the x-ray-diffraction experiments for $x=0.33$ in the starting powder. Large areas of $2\mathbf{a}_0\times2\mathbf{a}_0$ ordered superlattice are observed and this superlattice appears to be nearly perfect on a microscopic scale. Localized defects can be observed but these represent isolated defects in an otherwise perfect superlattice pattern. At Fe con-

centrations less than $x=0.33$ the areas of $2\mathbf{a}_0\times2\mathbf{a}_0$ superlattice gradually decrease and the $3\mathbf{a}_0\times3\mathbf{a}_0$ CDW superlattice appears. This is a gradual change in electronic structure with the detection of CDW structure in STM scans as soon as the Fe concentration of the starting powder is reduced below $x=0.20$.

The behavior of the energy gap in the conductance curves also shows a continuous slow change at the higher Fe concentrations and does not change appreciably in magnitude as the Fe concentration is increased to $x=0.33$. This indicates that both the low Fe concentration phases dominated by the CDW superlattice and the high Fe concentration phases dominated by the Fe superlattice formation exhibit an electronic spectrum with energy gaps of approximately equal magnitude. The persistence of a substantial energy gap can be interpreted as evidence for the existence of a density wave over the entire range of Fe concentrations.

It has already been suggested by Antoniou[12] that there is a competition between charge- and spin-density waves in transition-metal dichalcogenides and that the addition of Fe impurities helps to stabilize the spin-density wave (SDW). Using the framework of a Landau-Ginsburg mean-field theory he has developed a model for interpreting the behavior of 2H-Fe_xTaSe_2 based on the transition from a CDW to a CDWSDW phase. The latter is an aperiodic SDW stabilized by the Fe impurities with a smeared CDW serving as a background. This model was used to explain the nonlinear dependence of the Hall effect, the existence of a resistance maximum following a resistance minimum at low temperature, the negative magnetoresistance at high magnetic fields, and gives a good numerical fit to the susceptibility data on Fe_xTaSe_2 with $x\leq0.10$. The onset of the CDWSDW is predicted to be above 20 K for $x=0.10$ and to increase linearly with the concentration of Fe.

The model should be equally applicable to 2H-Fe_xNbSe_2 since the transport, magnetotransport, susceptibility, superlattice formation, and energy gaps behave in exactly the same way as observed for 2H-Fe_xTaSe_2. The only difference observed is that the STM detects a greater amplitude both at room temperature and at 4.2 K for the $2\mathbf{a}_0\times2\mathbf{a}_0$ superlattice formed in Fe_xNbSe_2 than formed in Fe_xTaSe_2, while the AFM shows equal amplitudes for the $2\mathbf{a}_0\times2\mathbf{a}_0$ superlattices in both materials at room temperature. This suggests a subtle difference in the bound charge transfer versus modification of the LDOS as detected by the STM.

The susceptibility data[4] indicate a transition to an antiferromagnetic state above $x=0.20$ and at $x=0.33$ a well-defined susceptibility maximum is observed at ~130 K. For dilute alloys with $x\leq0.07$ the negative magnetoresistance data[7] have also been fit to a theory by Beál-Monod and Weiner[13] and the required exchange constants are negative indicating an antiferromagnetic interaction.

Overhauser[14] originally proposed the formation of a static spin-density wave (SDW) as a possible mechanism for antiferromagnetism in dilute alloys. The paramagnetic solute atoms would then become oriented through their exchange interaction with the spin-density wave. 2H-$NbSe_2$ has nested Fermi surface sections which favor the formation of a CDW in the pure phase, but the intercalated magnetic impurities could tend to suppress the CDW component and stabilize the SDW component which at higher concentrations could drive the formation of an antiferromagnetic phase. The existence of a density-wave, either SDW or mixed SDWCDW, would explain the existence of the energy gap up to high Fe concentrations as observed in the STM spectroscopy experiments.

The STM and AFM scans are dominated at high Fe concentrations by the effects of the charge transfer to the Nb atoms by the Fe located below the Nb atoms in the octahedral holes and the resulting charge transfer to the surface Se atoms which gives rise to the dominant $2\mathbf{a}_0\times2\mathbf{a}_0$ superlattice. The density wave, either SDW or SDWCDW would exist at a wavelength determined by the Fermi surface nesting, possibly near $3\mathbf{a}_0$ as observed for the original CDW or at some other multiple of the lattice vector depending on the degree of Fermi surface modification due to Fe. The STM would not detect a dominant SDW and would have difficulty detecting a weak CDW component compared to the $2\mathbf{a}_0$ modulation associated with the direct static charge transfer to the surface Se.

B. Superlattice formation and STM spectroscopy of 2H-Fe_xTaSe_2

The behavior of 2H-Fe_xTaSe_2 as a function of Fe concentration is very similar to that observed for 2H-Fe_xNbSe_2. For more dilute concentrations the $3\mathbf{a}_0\times3\mathbf{a}_0$ CDW superlattice is still observed and the energy gap, after an initial reduction, changes very slowly as the Fe concentration is increased. A Kondolike resistance minimum and negative magnetoresistance are observed for $x\leq0.10$. These features disappear at high concentrations where a strong $2\mathbf{a}_0\times2\mathbf{a}_0$ superlattice appears. However, the onset of the magnetic transition in $Fe_{0.33}TaSe_2$ occurs at a substantially lower temperature than observed in $Fe_{0.33}NbSe_2$, 58 K versus 122 K. The STM modulation amplitude contributed by the $2\mathbf{a}_0\times2\mathbf{a}_0$ superlattice at 4.2 K is also substantially weaker in $Fe_{0.33}TaSe_2$, 0.25 Å versus 1.0 Å in $Fe_{0.33}NbSe_2$.

This comparison suggests that the modification in the LDOS at 4.2 K produced by the $2\mathbf{a}_0\times2\mathbf{a}_0$ superlattice in the antiferromagnetic phase is substantially weaker in $Fe_{0.33}TaSe_2$ than observed in $Fe_{0.33}NbSe_2$. The comparison of STM scans at room temperature also shows a much weaker modification in the LDOS for $Fe_{0.33}TaSe_2$.

In contrast to the STM profiles, the AFM profiles at room temperature show nearly identical absolute and relative amplitudes indicating that the total charge modification is the same in both materials. The conclusion is that $Fe_{0.33}NbSe_2$ shows a greater modification in the conduction electron LDOS while $Fe_{0.33}TaSe_2$ shows a greater static charge transfer associated with the Fe superlattice. In both materials at 4.2 K the LDOS is modulated by Fe and the persistence of the energy gap

structure over the entire range of Fe concentration suggests that a density wave is continuously present in the electron gas in both materials. The model of Antoniou[12] shows a satisfactory fit to the data on Fe_xTaSe_2 for $x \leq 0.10$, but has not been extended in any detail to the ordered magnetic phase.

The negative magnetoresistance fits to the Béal-Monod and Weiner[13] theory give negative exchange constants similar to those generated for Fe_xNbSe_2. However, the susceptibility has not been measured for the high Fe concentrations above $x = 0.20$.

C. Superlattice formation and STM spectroscopy of 2H-Fe_xTaS_2

For dilute concentrations of Fe in 2H-TaS_2 the effects on the transport properties are quite different from those observed for 2H-$NbSe_2$ and 2H-$TaSe_2$. At $x \approx 0.05$ a superconducting transition is observed at ~ 3 K in Fe_xTaS_2, but at 4.2 K an energy gap of 52.6 ± 2.2 meV is observed indicating that the CDW remains strong. This suggests that the CDW and superconductivity coexist at the lowest temperatures in 2H-$Fe_{0.05}TaS_2$. At higher temperatures the resistance rises monotonically and no Kondolike minima are observed (see Fig. 16). As the Fe concentration is increased, the CDW energy gap slowly decreases as larger regions of ordered Fe superlattice are formed.

The regions of Fe superlattice observed in the STM scans show two different geometries and these show a major difference in the energy gaps detected by STM spectroscopy. In regions of the crystal where a strong $2\mathbf{a}_0 \times 2\mathbf{a}_0$ superlattice is observed at high Fe concentrations, the energy gap remains fairly large and well defined at a value of 38.3 ± 2.0 meV as shown in the lower curve of Fig. 20. The same behavior was observed for the $2\mathbf{a}_0 \times 2\mathbf{a}_0$ superlattices in 2H-$Fe_{0.33}NbSe_2$ and 2H-$Fe_{0.33}TaSe_2$. In regions of the 2H-$Fe_{0.33}TaS_2$ crystals where a strong $\sqrt{3}\mathbf{a}_0 \times \sqrt{3}\mathbf{a}_0$ superlattice is observed little or no energy gap can be observed by STM spectroscopy as was shown in the upper curve of Fig. 20.

For 2H-Fe_xTaS_2 with $x = 0.33$ in the starting powder the dominant superlattice forming in the sintered powder as determined by x-ray diffraction[11] was $\sqrt{3}\mathbf{a}_0 \times \sqrt{3}\mathbf{a}_0$. Electron diffraction[9] on crystals grown from $x = 0.33$ powder also showed a clear $\sqrt{3}\mathbf{a}_0 \times \sqrt{3}\mathbf{a}_0$ superlattice, but the stoichiometry of the crystals as determined by x-ray fluorescence was $x = 0.28$, indicating a nonuniform Fe content. The STM scans on crystals also grown from $x = 0.33$ powder show regions of both $\sqrt{3}\mathbf{a}_0 \times \sqrt{3}\mathbf{a}_0$ and $2\mathbf{a}_0 \times 2\mathbf{a}_0$ superlattice, also indicating a nonuniform Fe content.

Magnetization measurements[9] and Mössbauer adsorption measurements[9] on $Fe_{0.28}TaS_2$ single crystals at 4.2 K showed the response to be ferromagnetic with a large coercive force and anisotropy. The x-ray and electron diffraction measurements suggest that these crystals are dominated by the $\sqrt{3}\mathbf{a}_0 \times \sqrt{3}\mathbf{a}_0$ superlattice so that the ferromagnetic phase of the crystal should be associated with the ordered $\sqrt{3}\mathbf{a}_0 \times \sqrt{3}\mathbf{a}_0$ superlattice.

The present STM and AFM results show that although the $\sqrt{3}\mathbf{a}_0 \times \sqrt{3}\mathbf{a}_0$ superlattice may dominate in crystals grown from $x = 0.33$ powder, microscopic regions of $2\mathbf{a}_0 \times 2\mathbf{a}_0$ superlattice can also be formed in such crystals. These regions exhibit a large energy gap in the electronic spectrum, comparable in magnitude to the energy gaps observed for the $2\mathbf{a}_0 \times 2\mathbf{a}_0$ Fe superlattices observed in 2H-Fe_xNbSe_2 and 2H-Fe_xTaSe_2. This also indicates the formation of a density wave in such regions. In this case the $2\mathbf{a}_0 \times 2\mathbf{a}_0$ superlattice would be antiferromagnetic and the $\sqrt{3}\mathbf{a}_0 \times \sqrt{3}\mathbf{a}_0$ superlattice ferromagnetic, a possibility since the exchange interaction can be a sensitive function of distance. In the bulk crystals the ferromagnetic phase would dominate properties such as magnetization.

V. CONCLUSIONS

The STM results have shown that the CDW modulation and CDW energy gaps in the 2H phases of Fe_xNbSe_2, Fe_2TaSe_2, and Fe_xTaS_2 persist up to relatively high concentrations of Fe, on the order of $x = 0.10$ to 0.20. At higher Fe concentrations the CDW modulation in the STM scans is replaced by a superlattice due to the ordered Fe occupancy in the octahedral holes in the van der Waals gap. When this superlattice is $2\mathbf{a}_0 \times 2\mathbf{a}_0$ a large energy gap in the electronic spectrum continues to be observed up to $x = 0.33$. This suggests the continued presence of a density wave at high Fe concentrations. A mechanism as originally proposed by Overhauser,[14] and a similar one developed later by Antoniou[12] could be operating. The stabilization of a static SDW would drive the formation of the antiferromagnetic phase, or the formation of a mixed SDWCDW could lead to the antiferromagnetic phase. The mixed density wave state has been discussed by Denley and Falicov[15] who studied a variety of electron correlated density wave states in hexagonal layers. When the Fe superlattice forms a $\sqrt{3}\mathbf{a}_0 \times \sqrt{3}\mathbf{a}_0$ lattice as observed for 2H-$Fe_{0.33}TaS_2$, the energy gap is no longer observed in the superlattice phase. This phase is also ferromagnetic and would not be characterized by a SDW or a mixed SDWCDW.

The STM and AFM scans indicate a rather large charge transfer to the surface Se or S atoms. This charge transfer is concentrated on one surface atom, but can be shared between the three surface Se or S atoms that were originally symmetrically located above the metal atom and the octahedral hole occupied by the Fe. Comparison of the STM and AFM scans shows that both the LDOS at the Fermi level and the static charge on the surface atoms are modified by Fe. The changes vary in both absolute and relative magnitude for the three materials studied and are strongest in 2H-$Fe_{0.33}NbSe_2$ where the antiferromagnetic transition shows the highest onset temperature of 122 K.

The use of the STM and AFM to study the new phases of the 2H layer structure dichalcogenides induced by intercalated Fe continues the use of probe microscopy studies that have proved very useful in looking at the most detailed structure in these materials. Recent results on 1T-TaS_2 were able to show the clear existence of domain

structure due to CDW formation. Wu and Lieber[16,17] showed the detection of CDW domain structure in 1T-TaS_2 using STM scans at room temperature. Burk *et al.*[18] using Fourier transforms of large area STM scans at room temperature were able to analyze both phase and amplitude characteristics of the CDW domain structure in 1T-TaS_2. Coleman, McNairy, and Slough[19] were able to analyze detailed amplitude variations due to CDW domains in real space STM data and to take into account interference effects from the atomic surface structure. All of these studies have demonstrated the power of scanning probe microscopes in detecting both surface structure and electronic structure.

The results reported here show that the combined use of STM, AFM, and STM spectroscopy can detect not only the microscopic superlattice formation due to Fe doping, but also provides clear evidence of a sequence of unusual electronic structure changes associated with increasing Fe concentration and the existence of density waves over the whole range of Fe concentration.

ACKNOWLEDGMENTS

The authors would like to thank Professor L. M. Falicov and Professor V. Celli for many useful discussions. Dr. W. M. McNairy contributed substantially to the crystal growth program. This research was supported by the Department of Energy Grant No. DE-FG05-84ER4507.

[1]J. A. Wilson and A. D. Yoffe, Adv. Phys. **18**, 193 (1969).
[2]J. A. Wilson, F. S. DiSalvo, and S. Majahan, Adv. Phys. **24**, 117 (1975).
[3]R. V. Coleman, Zhenxi Dai, W. W. McNairy, C. G. Slough, and Chen Wang, in *Surface Properties of Layered Structures,* edited by G. Benedek (Kluwer Academic, The Netherlands, 1992), pp. 27–95.
[4]R. V. Coleman, B. Giambattista, P. K. Hansma, A. Johnson, W. W. McNairy, and C. G. Slough, Adv. Phys. **37**, 559 (1988).
[5]Digital Instruments, Inc., 6780 Cortona Drive, Santa Barbara, CA 93117.
[6]D. E. Moncton, J. D. Axe, and F. J. DiSalvo, Phys. Rev. Lett. **34**, 734 (1975).
[7]D. A. Whitney, R. M. Fleming, and R. V. Coleman, Phys. Rev. B **15**, 3405 (1977).
[8]S. J. Hillenius and R. V. Coleman, Phys. Rev. B **20**, 4569 (1979).
[9]M. Eibschütz, F. J. DiSalvo, G. W. Hull, Jr., and S. Majahan, Appl. Phys. Lett. **27**, 464 (1975).
[10]J. M. Vorhoeve, Née van den Berg, and M. Robbins, J. Solid State Chem. **1**, 134 (1970).
[11]J. M. van den Berg and P. Cossee, Inorg. Chim. Acta **2**, 143 (1968).
[12]P. D. Antoniou, Phys. Rev. B **20**, 231 (1979).
[13]M. T. Béal-Monod and R. A. Weiner, Phys. Rev. **170**, 552 (1968).
[14]A. W. Overhauser, Phys. Rev. B **29**, 7023 (1984).
[15]D. Denley and L. M. Falicov, Phys. Rev. B **17**, 1289 (1978).
[16]Xian-Liang Wu and Charles M. Lieber, Science **243**, 1703 (1989).
[17]Xian-Liang Wu and Charles M. Lieber, Phys. Rev. Lett. **64**, 1150 (1990).
[18]B. Burk, R. E. Thomson, A. Zettl, and John Clarke, Phys. Rev. Lett. **66**, 3040 (1991).
[19]R. V. Coleman, W. W. McNairy, and C. G. Slough, Phys. Rev. B **45**, 1428 (1992).

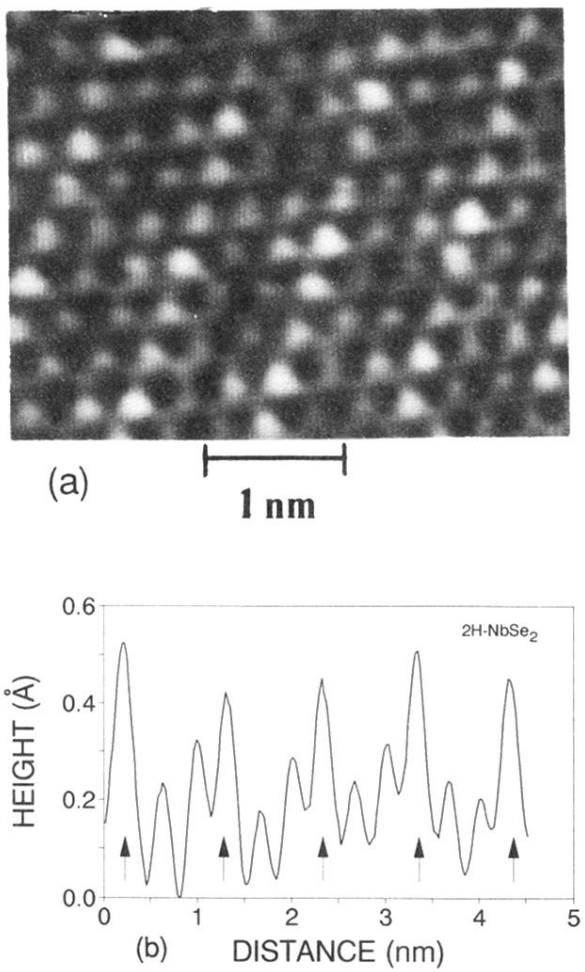

FIG. 1. (a) STM gray scale image of 2H-$NbSe_2$ recorded at 4.2 K (2 nA, 50 mV). This shows a $\sim 3\mathbf{a}_0 \times 3\mathbf{a}_0$ CDW superlattice. (b) Profile of z deflection along a line of atoms in (a). The total z deflection is ~ 0.5 Å with the CDW and atomic modulations showing approximately equal magnitudes (from Ref. 4).

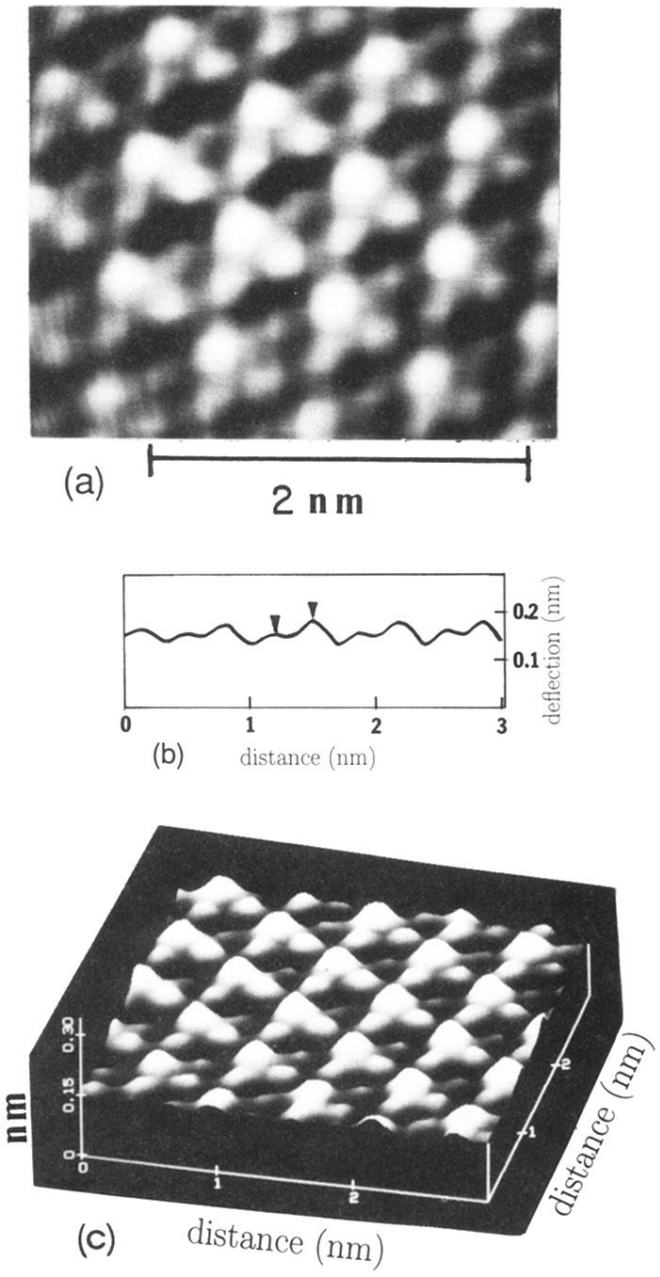

FIG. 10. (a) Gray scale image of AFM scan at room temperature on 2H-$Fe_{0.33}NbSe_2$. The image was recorded using the constant force mode. The image shows a basic $2\mathbf{a}_0 \times 2\mathbf{a}_0$ structure, but with a stronger three atom cluster than observed in the STM scan. (b) Profile of z deflection for the AFM scan of (a). The profile indicates that the atomic and superlattice deflections are comparable. (c) Three-dimensional projection of the AFM scan of (a). The strong three-atom cluster is clearly evident.

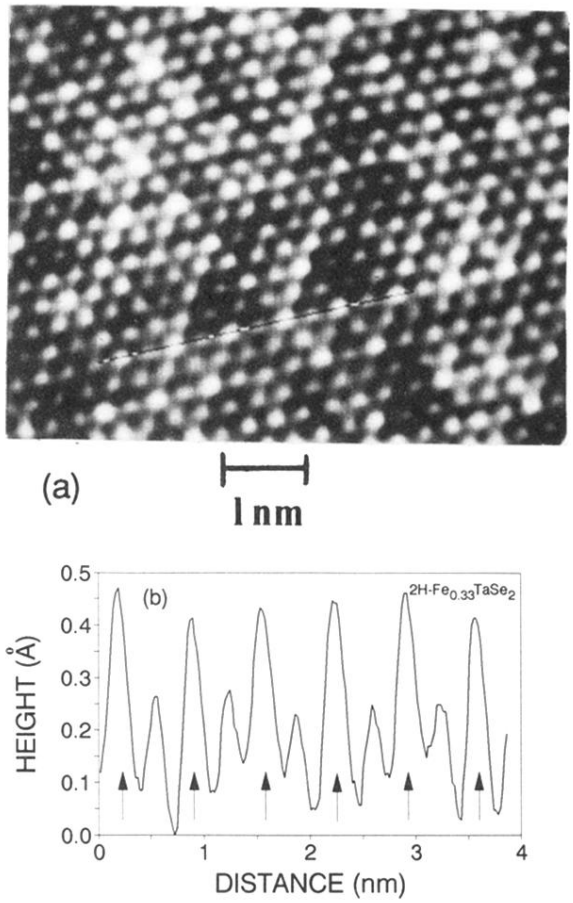

FIG. 14. (a) STM gray scale image of 2H-$Fe_{0.33}TaSe_2$ recorded at 4.2 K (2 nA, 50 mV). A $2\mathbf{a}_0 \times 2\mathbf{a}_0$ superlattice is clearly seen. (b) Profile of z deflection along the line shown in (a). The total z deflection is ~ 0.5 Å with superlattice and atomic modulations of approximately equal amplitudes.

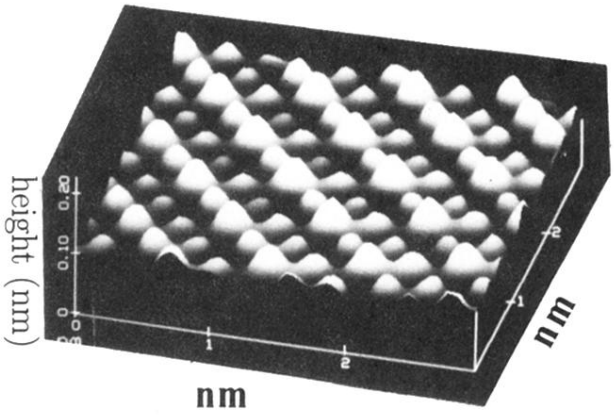

FIG. 15. Three-dimensional projection of an AFM scan at room temperature on 2H-$Fe_{0.33}TaSe_2$. The picture was recorded using the constant force mode. The picture indicates a clear $2\mathbf{a}_0 \times 2\mathbf{a}_0$ superlattice due to the Fe intercalation.

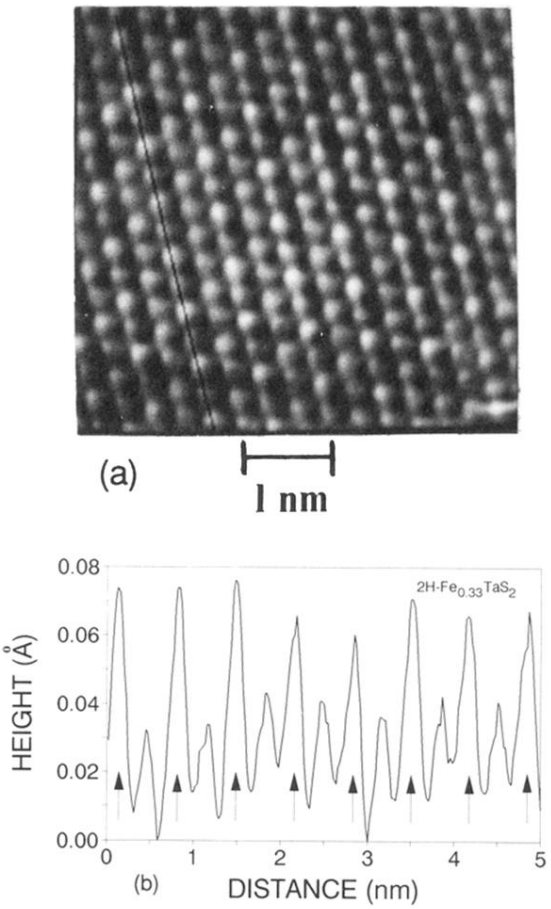

FIG. 17. (a) STM gray scale image of 2H-$Fe_{0.33}TaS_2$ recorded at 4.2 K (2 nA, 50 mV). A complete $2\mathbf{a}_0 \times 2\mathbf{a}_0$ superlattice is clearly seen. (b) Profile of z deflection along the line shown in (a). The total z deflection is ~ 0.07 Å with the superlattice and atomic modulations of approximately equal amplitudes. These are much weaker than observed for pure 2H-TaS_2.

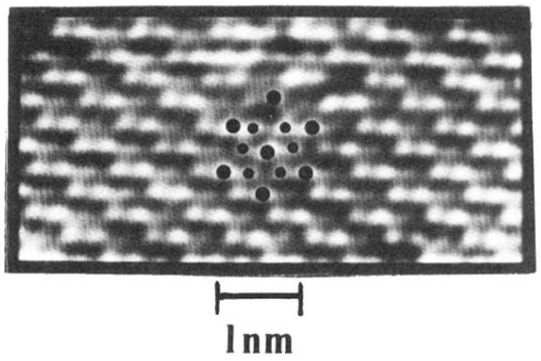

FIG. 19. STM gray scale image of 2H-$Fe_{0.33}TaS_2$ recorded at 4.2 K. A $\sqrt{3}\mathbf{a}_0 \times \sqrt{3}\mathbf{a}_0$ superlattice is observed. The superlattice, marked by larger solid circles, appears as the larger hexagon rotated 30° from the inner atom hexagon (small solid circles).

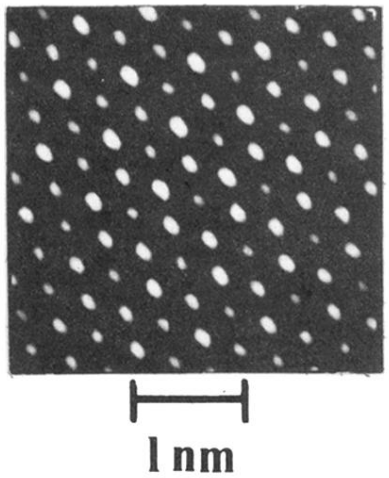

FIG. 21. Gray scale image of AFM scan at room temperature on 2H-$Fe_{0.33}TaS_2$. The image was recorded using the constant force mode. The upper region shows a large bright hexagon with an inner weaker hexagon rotated by 30°, while the lower region shows a large weak hexagon with an inner brighter hexagon rotated by 30°. This indicates a phase slip of the $\sqrt{3}\mathbf{a}_0 \times \sqrt{3}\mathbf{a}_0$ superlattice, created by an increase in the local concentration of Fe in the octahedral holes.

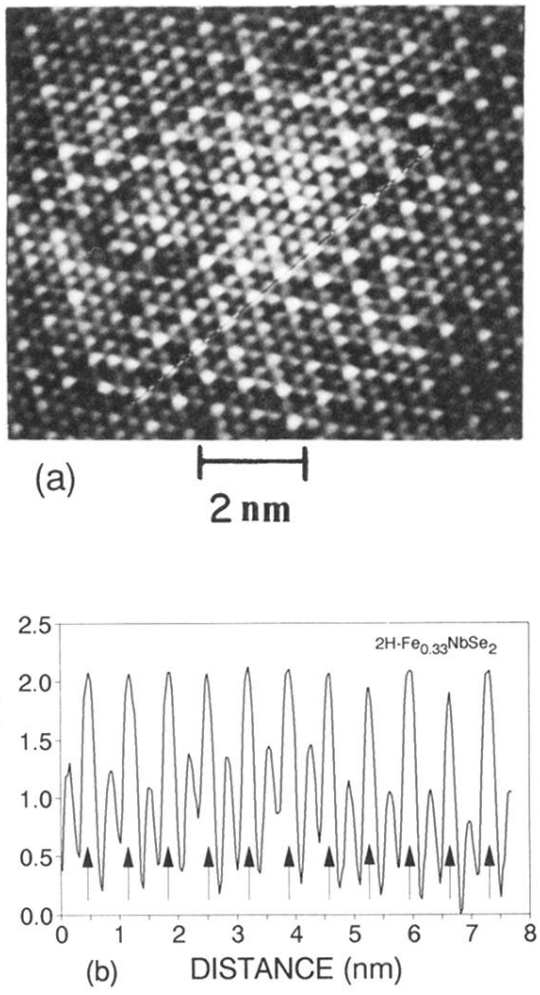

FIG. 6. (a) STM gray scale image of 2H-$Fe_{0.33}NbSe_2$ recorded at 4.2 K (2 nA, 50 mV). A $2\mathbf{a}_0 \times 2\mathbf{a}_0$ superlattice is clearly seen, which indicates that the $\sim 3\mathbf{a}_0 \times 3\mathbf{a}_0$ CDW superlattice is reduced or converted to a mixed density wave. (b) Profile of z deflection along the line shown in (a). The total z deflection is ~ 2 Å with superlattice and atomic modulations of approximately equal amplitudes. However, these are much larger than those observed for pure 2H-$NbSe_2$.

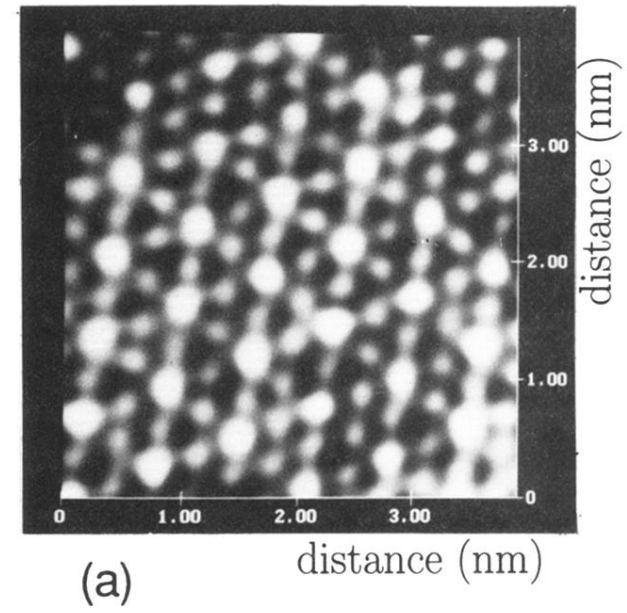

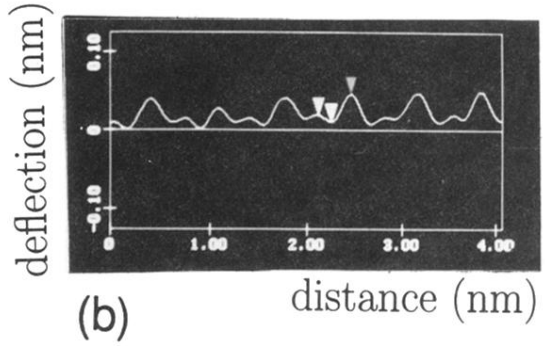

FIG. 9. (a) Gray scale image of STM scan at room temperature on 2H-$Fe_{0.33}NbSe_2$. The image was recorded using the constant current mode with $V=20$ mV and $I=6$ nA. The image indicates enhanced amplitude on every other Se atom with a slight asymmetry emphasizing two additional surface Se atoms in the seven atom cluster. (b) Profile of z deflection along a row of atoms in (a).